Journal of Electronic Materials (2021) 50:3722–3730
https://doi.org/10.1007/s11664-021-08889-6

ORIGINAL RESEARCH ARTICLE

Enhancing Detectivity of Indium-Oxide-Based Photodetectors via Vertical Nanostructuring Through Glancing Angle Deposition

Amitabha Nath[1] · Bikram Kishore Mahajan[2] · Laishram Robindro Singh[3] · Shubhajit Vishwas[1] · Rajib Kumar Nanda[1] · Mitra Barun Sarkar[1]

Received: 13 October 2020 / Accepted: 16 March 2021 / Published online: 15 April 2021
© The Minerals, Metals & Materials Society 2021

Abstract

In_2O_3 vertical nanostructures (VNS) are fabricated using a glancing angle deposition (GLAD) technique upon an In_2O_3 thin film (TF) on a n-type silicon (n-Si) substrate. Analysis using high-resolution transmission electron microscopy (HRTEM) and high-resolution x-ray diffraction (HRXRD) revealed that the In_2O_3 VNS are amorphous in nature. An average ~4.5-fold enhancement in absorption was observed and a microscopic origin was proposed for observed bandgap changes for the n-Si/In_2O_3 TF/GLAD In_2O_3 VNS and bare n-Si/In_2O_3 TF samples in the visible region due to surface-related trap states or oxygen vacancies. The improvement in photodetection was attributed to the presence of a large number of surface-related trap states at the edge of metal contacts. The fabricated VNS detector possesses enhanced photosensitivity (~1.7-fold) due to an efficient photogating effect in the depletion region. A maximum detectivity of ~12.8 × 10^7 Jones was observed for the n-Si/In_2O_3 TF/GLAD In_2O_3 VNS device, which possesses ~15.6-fold enhanced detectivity as compared to the bare n-Si/In_2O_3 TF device.

Graphic Abstract

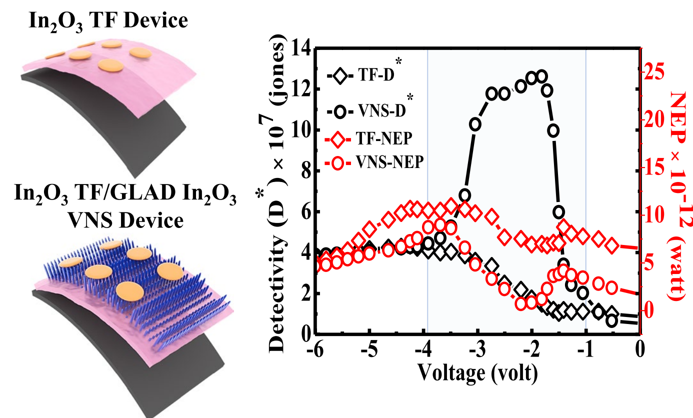

Keywords Indium oxide · glancing angle deposition · nanostructures · optical absorption · photodetection · detectivity

✉ Mitra Barun Sarkar
mbarun.ece@nita.ac.in

[1] Department of Electronics and Communication Engineering, National Institute of Technology, Agartala, West Tripura 799046, India

[2] School of Electrical and Computer Engineering, Purdue University, West Lafayette, IN 47907, USA

[3] Department of Nanotechnology, North Eastern Hill University, Umshing, Mawkynroh, Shillong, Meghalaya 793022, India

Introduction

One of the major drivers in modern technologies, which has transformed every aspect of our life in recent times, is optoelectronic devices, including photodetectors. Photodetectors convert light into electrical signals, and have found applications in various fields, like early detection of tumors[1] optical communications,[2] astronomy,[3] and medical imaging.[4] With

the semiconductor industry stretching Moore's law to its limit, such as in the case of Samsung's 3-nm-gate-all-around transistor,[5] the miniaturization of photodetectors is the need of the hour, so that they can be integrated with the state-of-art CMOS processors. At the same time, the search for materials and structures with improved photodetection properties has been a huge priority. Indium oxide (In_2O_3), which is a low-cost, wide-bandgap (~3.6 eV), highly conducting and transparent metal-oxide semiconductor,[6] has been a material of choice. Recent reports on In_2O_3 have demonstrated enhanced optical and electrical properties[7] but involve surface micromachining techniques and multi-step fabrication techniques like sputtering and electron beam evaporation, which makes it too costly to be commercially produced.

Glancing angle deposition or GLAD is an attractive option for fabricating In_2O_3 photodetectors because, in addition to being a reliable, sophisticated technique with *in-situ* characterization and control, it is a cheap, one-step process without the need for secondary steps such as annealing or etching. GLAD has also been used previously for the fabrication of In_2O_3 nanostructures[7] for photodetectors.[8]

Nanowires (NWs) are very appealing for photodetectors due to their high surface-area-to-volume ratio and Debye length compared to their sizes, and highly controllable growth using advanced techniques like GLAD. Combining In_2O_3 NWs with TiO_2 NWs, which are themselves good photodetectors,[9] can further boost the efficiency of the photodetector. In this paper, an In_2O_3 TF/GLAD In_2O_3 VNS device was demonstrated. The In_2O_3 TF, while functioning as an adhesion layer for the In_2O_3 VNS due to better lattice matching, also increases the active area of the device, thus playing a critical role in device performance and stability. In literature, a bare In_2O_3 TF has already been successfully used for photodetection.[10] Therefore, to understand and quantify the improvement in photodetection due to the VNS, the electrical and optical properties of the current device (n-Si/In_2O_3 TF/GLAD In_2O_3 VNS) were compared to the bare In_2O_3 TF device. One major advantage that the n-Si/In_2O_3 TF/GLAD In_2O_3 VNS device possesses is visible detection, compared to ultra-violet detection in the case of an In_2O_3 VNS[8] device, thus making our device more attractive for integration with commercial off-the-shelf devices.

Experimental

Fabrication of GLAD In_2O_3 VNS Device

The n-type Silicon (n-Si) substrates were cleaned with tetrachloroethylene (C_2Cl_4), methanol (CH_3OH), Acetone (C_3H_6O) and DI water (H_2O), before fabrication. A solution of hydrofluoric acid (HF) + DI water (H_2O) was used at a volume ratio of 1:50 to etch the native oxide from the Si substrate. The GLAD technique was used to fabricate the In_2O_3 TF (~70 nm)/In_2O_3 VNS (~400 nm) device on the pre-cleaned n-type Si <100> substrate (resistivity <30 Ω-cm), using In_2O_3 (highly pure 99.999%, MTI Corporation, USA) source material, at a high vacuum chamber pressure of 2×10^{-8} bar using an electron beam (Hind High Vacuum Co. (p) Ltd., 15F6) evaporator. A representative schematic of the fabricated device is shown in Fig. 1. An indium (In) contact (contact area ~1.96×10^{-6} m^2) was deposited through an aluminum mask hole. The deposition rates were maintained at 0.12 nm/s for both the TF and VNS. The distance from the substrate holder to the material source was kept at ~25 cm with >80° GLAD orientation, and azimuthal rotation was fixed at ~130 rpm. The two devices thus fabricated are (1) n-Si/In_2O_3 TF and (2) n-Si/In_2O_3 TF/GLAD In_2O_3 VNS.

Device Characterization

The field emission scanning electron microscopy (FESEM) and corresponding EDS (Carl Zeiss, Sigma) chemical mapping were done to study sample morphology and confirm the presence of different elements on the samples. The growth of VNS was characterized by high-resolution transmission electron microscopy (HRTEM) (JEOL JEM-200 KV, Model No. JEE- 2100) and corresponding selected area electron diffraction (SAED). The structural analysis was done by high-resolution x-ray diffraction (HRXRD) (Bruker D8 Advance). The optical absorption measurement was done using a UV-Vis spectrophotometer (Lambda 950, Perkin Elmer). The current (*I*)-voltage (*V*) characteristics were obtained using a Keysight B2902A source and measurement unit (SMU) with a tungsten filament source.

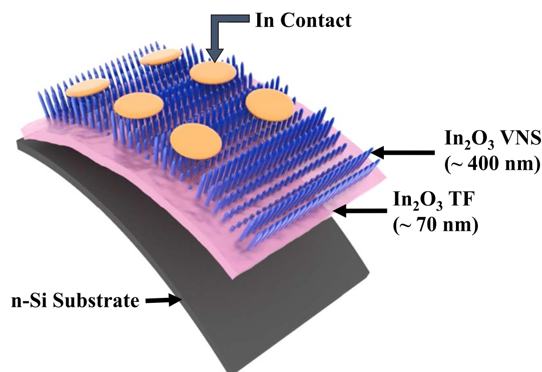

Fig. 1 Schematic diagram of n-Si/In_2O_3 TF/GLAD In_2O_3 VNS device.

Results and Discussion

Morphological Analysis

Figure 2 shows the FESEM and HRTEM images of the samples fabricated by the GLAD technique. Figure 2a shows a top view of the In_2O_3 VNS (with an inset cross-sectional view of the VNS) fabricated on In_2O_3 TF using the GLAD technique. The top-view FESEM image shows that the clusters of VNS are all over the sample, and the cross-sectional view also confirms the formation of the clusters of VNS. The VNS also show a prominent geometric shadowing effect which is a signature of the GLAD technique. As deposition proceeds inside the GLAD chamber, short islands of VNS are shadowed by tall islands, as a result of which the tall islands keeps growing, while the short islands don't receive much flux, giving rise to these unique structures.[11] It can be seen from the cross-sectional FESEM image that the VNS are densely packed all over the TF surfaces, and the upper surface of the VNS is extremely uneven. The formation of VNS was due to the perpendicular components of the incident vapor flux and constant rotation of the GLAD system, which depends on vacuum pressure, evaporation rate, rotation speed, glancing angle, and material-melting current.[12,13] The high substrate temperature (~15°C) results in a large diffusion coefficient, which aids the growth of VNS.[14] Figure 2b shows a top view of the In_2O_3 TF substrate. The relatively 'featureless' FESEM image implies the uniform deposition of In_2O_3 film all over the n-Si substrate. During evaporation, the In_2O_3 may get segregated into indium (In) and oxygen (O) molecules, which was confirmed by the EDS spectra in Fig. 2c (inset: sample selected area and chemical mapping). The chemical mapping of the sample showed the presence of In L (blue color), O K (green color) with an atomic ratio of In:O = 1.5:1 and native Si substrate. Figure 2d shows the HRTEM image of In_2O_3 VNS, where the yellow arrow specified the growth direction of the VNS. In this figure, the dusky part of the VNS is due to the existence of silicon and the dazzling part indicates the presence of oxygen molecules. The inset Fig. 2d shows the selected

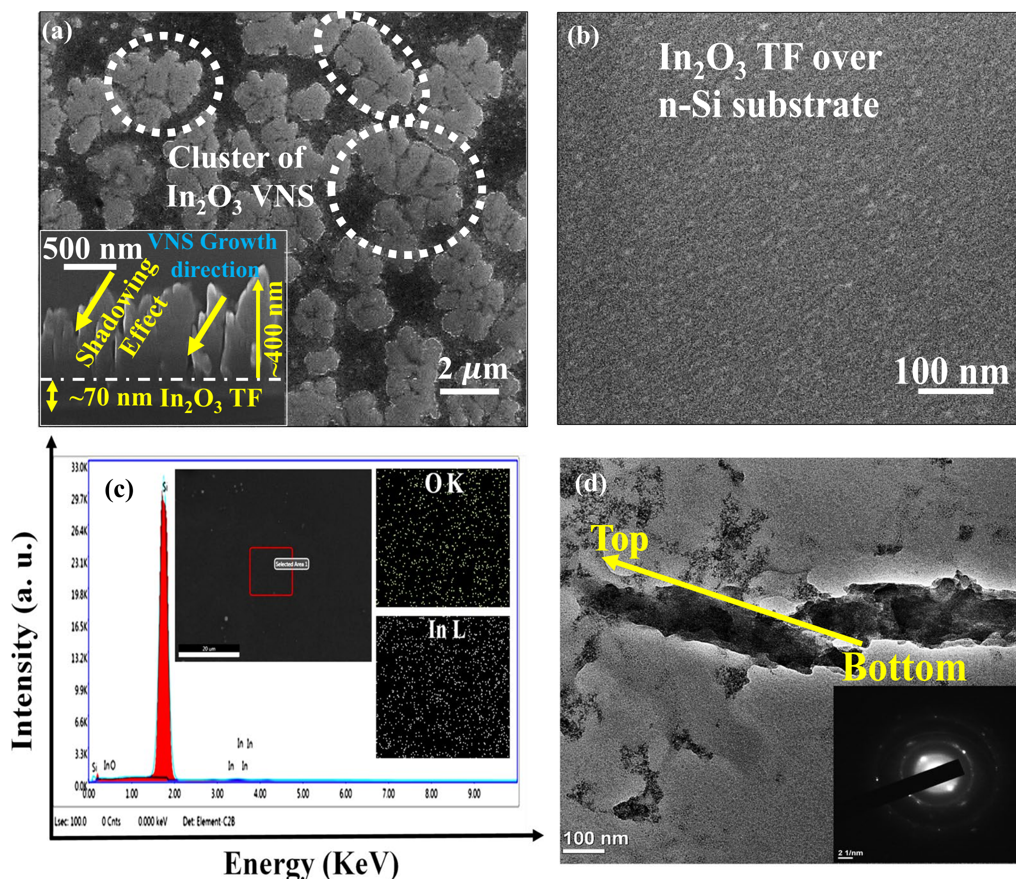

Fig. 2 (a) Top view FESEM images of the n-Si/In_2O_3 TF/GLAD In_2O_3 VNS (inset: cross-sectional view of VNS), (b) Top view FESEM images of the n-Si/In_2O_3 TF, (c) EDS spectrum (inset: sample selected area and chemical mapping), (d) HRTEM image of individual In_2O_3 VNS (inset: SAED patterns).

area diffraction (SAED) pattern of In_2O_3 VNS. The In_2O_3 VNS were deemed amorphous, as they show diffusive ring patterns and the absence of any fringe spacing.[15] The SAED pattern also shows the *d*-spacing of 2 Å, 1.1 Å, and 0.8 Å for the In_2O_3 VNS, which is close to the reported *d*-space value of In_2O_3 (JCPDS card no. 65-3170).

HRXRD Analysis

Figure 3 shows HRXRD patterns of the n-Si/In_2O_3 TF/GLAD In_2O_3 VNS and bare n-Si/In_2O_3 TF (inset Fig. 3) in the 2θ range of 30° to 75°. The diffraction planes (400), (422), (622), (444) at 2θ = 38.31°, 44.47°, 61.98°, 64.97° and (400), (422), (444) at 2θ = 38.31°, 44.55°, 64.89°, respectively, were identified as per JCPDS data (JCPDS card no. 06-0416).[16] The average grain size was calculated ~33 nm for n-Si/In_2O_3 TF and ~40 nm for n-Si/In_2O_3 TF/GLAD In_2O_3 VNS using the Debye-Scherrer equation, $D = (0.9\cdot\lambda)/(\beta\cos\theta)$.[17] Where λ, 2θ, β, D is the wavelength, Bragg's angle, full width at half maximum (FWHM), and average grain size, respectively. In the case of the VNS, the increased grain size may be attributed to the presence of a new diffraction plane of (622), which may form depending on the deposition rate, glancing angle, and substrate temperature.[18] The high substrate temperature used in our case prevents the atomic arrangement in crystalline size, which is corroborated by the SAED pattern in the HRTEM analysis.

Optical Absorption Analysis

The optical absorption of the n-Si/In_2O_3 TF/GLAD In_2O_3 VNS and as-deposited n-Si/In_2O_3 TF samples was measured at room temperature in the wavelength range of 330-660 nm, as depicted in Fig. 4a. The In_2O_3 VNS on top of the In_2O_3 TF acts as an anti-reflection coating, which enhances the optical absorption (~4.5-fold enhancement in the visible region) by increasing scattering of incident light. The enhancement can be further attributed to oxygen-related defects, which may have formed during the fabrication process, and which have different optical transition processes in the bandgap of the In_2O_3, which in turn increases photon absorption in all regions.[19] Figure 4b shows that the curve for the optical bandgap for n-Si/In_2O_3 TF and n-Si/In_2O_3 TF/GLAD In_2O_3 VNS, which was estimated at ~3.22 eV (Fig. 4c) by linear extrapolation from n-Si/In_2O_3 TF, corresponds to the main bandgap transition (the inset shows the subsequent absorption peak). Also, ~2.60 eV (Fig. 4d) and ~2.08 eV (Fig. 4e) correspond to the main bandgap and sub-bandgap transitions due to trapped electron-hole recombination at the oxygen vacancies[20] for the n-Si/In_2O_3 TF/GLAD In_2O_3 VNS (the inset shows the subsequent absorption peak). All the calculated optical bandgaps were at high optical absorption peaks.[17] The microscopic origin of the change of bandgap may be attributed to the oxygen-related defects, which may have been formed during the fabrication process. Such defect-related bandgap changes have been documented in other materials in the literature,[21–27] which in turn decreases the probability of electron-hole recombination in the material.

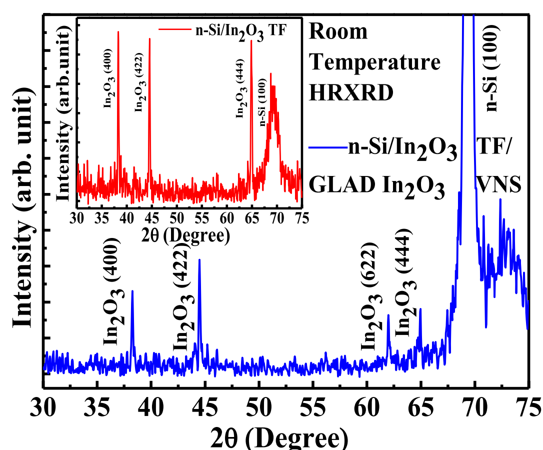

Fig. 3 HRXRD pattern of the n-Si/In_2O_3 TF/GLAD In_2O_3 VNS upon the n-Si substrate (inset: HRXRD pattern of n-Si/In_2O_3 TF).

The optical bandgap was determined by the method proposed by Jan Tauc *et al.*[28]

$$(\alpha h\nu) = A(h\nu - E_g)^n \tag{1}$$

where α is the absorption coefficient, $h\gamma$ is the incident photon energy, A is the proportionality constant, and E_g is the optical bandgap. The exponent 'n' takes the value of either ½ or 2 depending on whether the equation represents direct or indirect bandgap transitions.[17,29] The method of calculating the band at the absorption peaks[15,17,30] was followed here. The entire $(\alpha h\nu)^2$ versus $h\nu$ plot is shown in Fig 4b. However, the linear regions are extrapolated only at the peaks in the absorption spectra, as indicated by the arrows. The insets of Fig 4c, d and e show a magnified view of the absorption peak. The main bandgap and sub-bandgap transition are presumably due to the presence of a large number of surface trap states and/or oxygen vacancies. These vacancies can trap the photo-excited carriers and, in the process, play a major role in narrowing the bandgap inside the structures.[31]

Urbach's empirical rule[32,33] explains the modulation of the main bandgap and sub-bandgap transitions. The width of the absorption tail of defect states in the bandgap was assumed from the Urbach energy plot. When the samples are irradiated with a particular wavelength of light, the defect states trap the photo-excited carriers, which was the reason for the absorption tail appearing in the absorption spectra,[34] which is known as an Urbach tail and was also associated with the Urbach energy. According to the Urbach's empirical

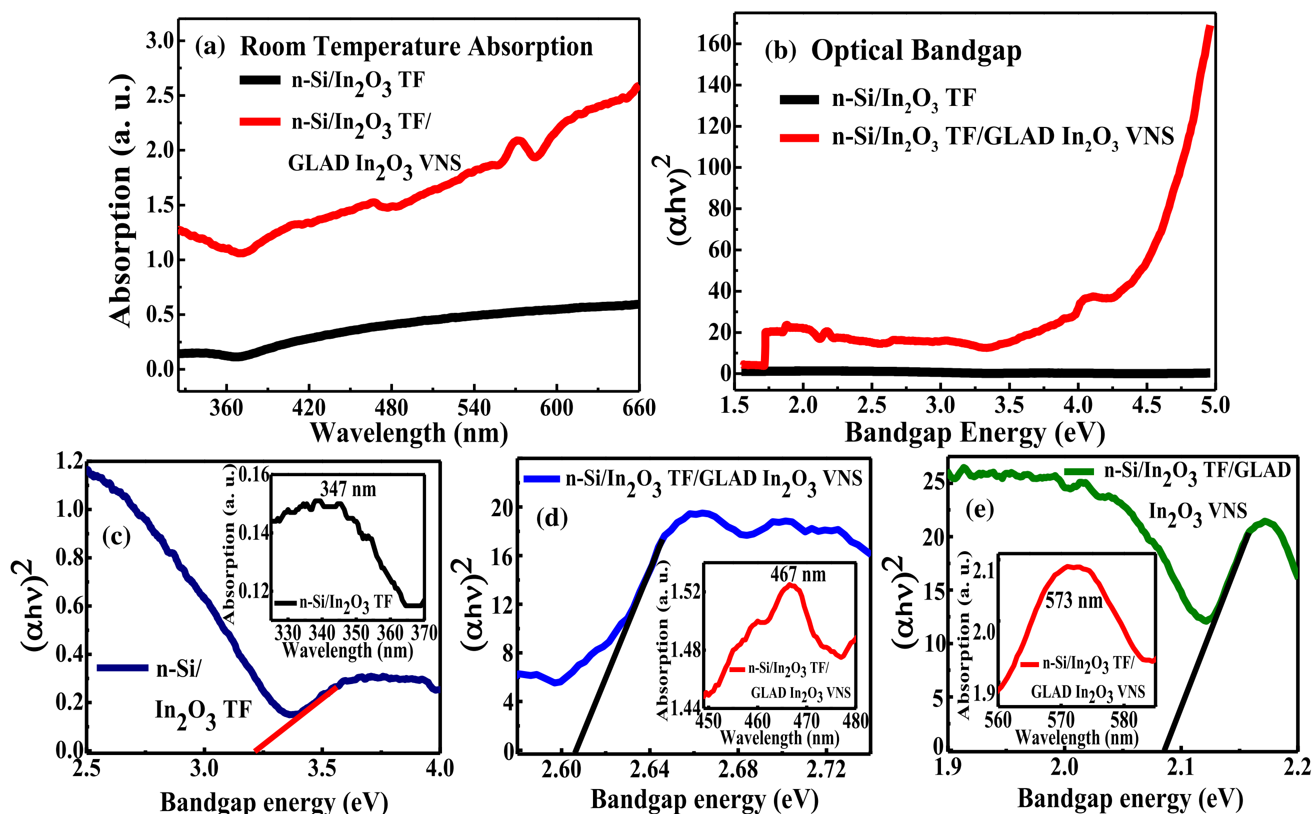

Fig. 4 (a) Room-temperature absorption spectra, (b) Entire $(\alpha h\nu)^2$ versus $h\nu$ curve for n-Si/In_2O_3 TF and n-Si/In_2O_3 TF/GLAD In_2O_3 VNS. Optical bandgap by linear extrapolation for (c) n-Si/In_2O_3 TF (inset: subsequent absorption spectrum), (d) n-Si/In_2O_3 TF/GLAD In_2O_3 VNS for main bandgap (inset: subsequent absorption spectrum), (e) n-Si/In_2O_3 TF/GLAD In_2O_3 VNS for sub-bandgap (inset: subsequent absorption spectrum).

rule, the equation for the Urbach energy was written using the below equations.

$$\alpha = \alpha_0 \exp\left(\frac{h\nu}{E_U}\right) \tag{2}$$

$$\ln(\alpha) = \ln(\alpha_0) + \left(\frac{h\nu}{E_U}\right) \tag{3}$$

where α, α_0, $h\nu$, and E_U is the absorption coefficient, a constant, incident photon energy, and the Urbach energy, respectively.[32] Here, the values of E_U are 0.57 eV and 1.62 eV for n-Si/In_2O_3 TF and n-Si/In_2O_3 TF/GLAD In_2O_3 VNS, which were found from the reciprocal of the slope of the linear part of *ln*(α) versus $h\nu$,[33] depicted in Fig. 5. The enhancement in the Urbach energy indicates the occurrence of a large number of defect states, disordered atoms, and interstitial states in the n-Si/In_2O_3 TF/GLAD In_2O_3 VNS sample.[34] The defect states, disordered atoms, and interstitial states introduced localized states near the conduction band, leading to an increase in the Urbach energy, and the Urbach tail or band tail width. Similar effects also have been reported by Chen *et al*. in ZnO film after doping with Cu and Ag.[35] On the other hand, the decrease in Urbach energy also indicates a reduction in defect states.[33] The bandgap and Urbach energy for both samples are tabulated in Table I.

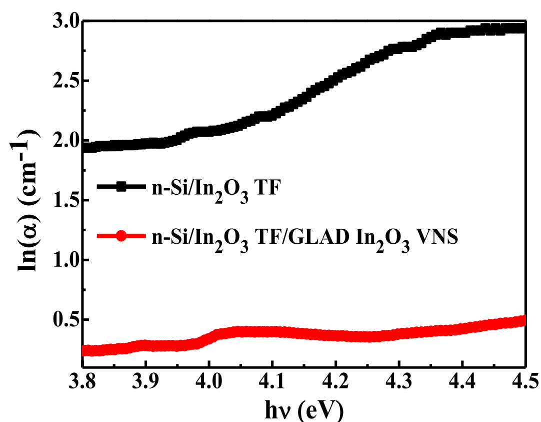

Fig. 5 Variation of Urbach energy with incident photon energy.

Photodetection Analysis

Figure 6a shows the semi-logarithmic *I–V* (*ln(I)–V*) characteristics for the n-Si/In_2O_3 TF and n-Si/In_2O_3 TF/GLAD In_2O_3 VNS devices determined using the Keysight B2902A SMU with a tungsten filament source at room temperature. Under dark conditions, the n-Si/In_2O_3 TF device shows a reverse breakdown voltage of −3 V which was reduced to −2.30 V under illumination. For the n-Si/In_2O_3 TF/GLAD In_2O_3 VNS device, however, the reverse breakdown observed at −2.50 V under dark conditions was reduced to −1 V under illumination. The maximum current was ~2.6 mA (dark) and ~2.9 mA (light) at −8 V for the n-Si/In_2O_3 TF device and ~2.2 mA (dark) and ~3.3 mA (light) at −8 V for the n-Si/In_2O_3 TF/GLAD In_2O_3 VNS device. The improved photocurrent in the n-Si/In_2O_3 TF/GLAD In_2O_3 VNS device was due to higher scattering of light inside the VNS structure[36] and the presence of oxygen-related trap states at the edge of metal contact,[30] as argued in the previous section. Also, under reverse-bias conditions, holes get trapped by the surface trap states[37] and oxygen-related trap states, which in turn reduces the depletion region in the structures and allows electron tunneling.[30] The ideality factor (η) of the diodes was extracted using the following equation.

Table I The extracted bandgaps and Urbach energy for n-Si/In_2O_3 TF and n-Si/In_2O_3 TF/GLAD In_2O_3 VNS samples

Sample	Main bandgap	Sub-bandgap	Urbach energy
n-Si/In_2O_3 TF	3.22 eV	–	0.57 eV
n-Si/In_2O_3 TF/GLAD In_2O_3 VNS	2.60 eV	2.08 eV	1.62 eV

$$\eta = \frac{1}{\frac{kT}{q}} \frac{\partial V}{\partial(\ln(I))} \quad (4)$$

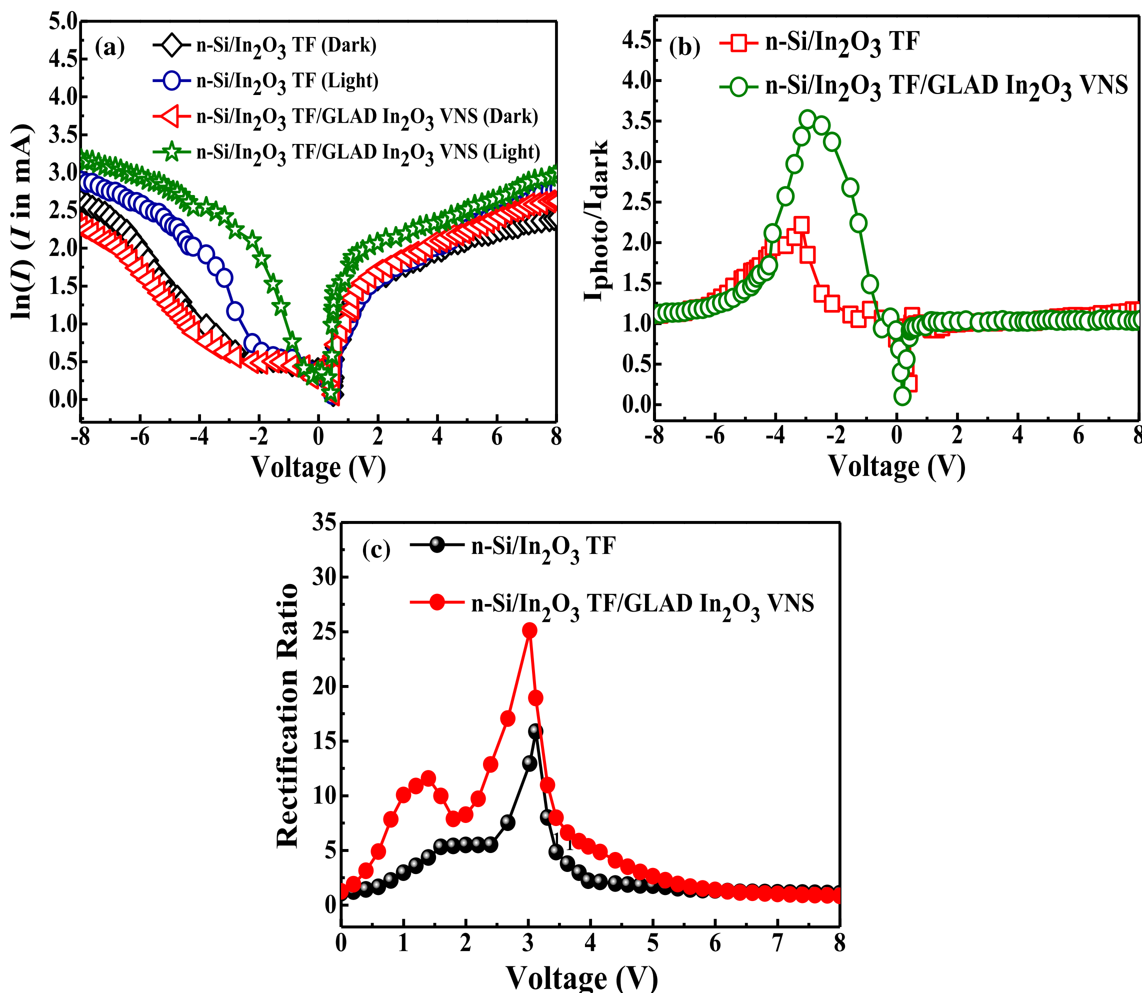

Fig. 6 (a) *ln(I)–V* characteristics for the n-Si/In_2O_3 TF and n-Si/In_2O_3 TF/GLAD In_2O_3 VNS detectors (inset: device structures), (b) photosensitivity of the devices, (c) rectification ratio.

where k is Boltzmann constant, T is the absolute temperature ($T = 300$ K), q is an electron charge and $\frac{\partial(\ln(I))}{\partial V}$ is the slope of the *ln(I)-V* curve.[38] The ideality factor (η) for both devices was ~15 and ~21 for n-Si/In_2O_3 TF and n-Si/In_2O_3 TF/GLAD In_2O_3 VNS, respectively, from Fig. 6a, which is less than the previously reported values.[11] The enhanced ideality may be due to carrier tunneling through the trap states between the oxide dielectric and the metal (In) contact,[39] and the efficient recombination of electrons and holes in the depletion region.[40] The photosensitivity (I_{photo}/I_{dark}) for both devices under the reverse-bias conditions are shown in Fig. 6b. A total ~1.7-fold enhancement in photosensitivity was observed for the n-Si/In_2O_3 TF/GLAD In_2O_3 VNS device at an applied voltage of −3 V. The enhancement in photosensitivity was attributed to the ample number of trap states which may have formed due to numerous dangling bonds over the nanostructured surface, which can easily attract oxygen molecules, hence the maximum electron tunneling happened at −3 V.[30,41]

The rectification ratio (R_{ratio}) of the two devices was calculated as shown in Fig. 6c. The R_{ratio} is defined as $\frac{|I_F|}{|I_R|}$, where I_F and I_R represent the forward and reverse dark current, respectively. At ~3 V, the R_{ratio} increased by ~1.6-fold in the case of the n-Si/In_2O_3 TF/GLAD In_2O_3 VNS device compared to the bare n-Si/In_2O_3 TF device. The R_{ratio} exhibits good rectifying behavior in the dark, which is attributed to high electron mobility in the n-Si/In_2O_3 TF/GLAD In_2O_3 VNS device.[42] Under the dark condition, the turn-on voltage of the n-Si/In_2O_3 TF/GLAD In_2O_3 VNS device is 1.5 V, whereas, for the n-Si/In_2O_3 TF device, it is 1 V. The reason behind the increased turn-on voltage could be that the In_2O_3 VNS acts as a blocking layer, thus increasing the turn-on voltage,[9] and as a result, the n-Si/In_2O_3 TF/GLAD In_2O_3 VNS device shows a better rectification ratio compared to the n-Si/In_2O_3 TF device.

The barrier height was ~0.60 eV and ~0.46 eV, respectively, at zero bias voltage at the n-Si/In_2O_3 TF interface and the n-Si/In_2O_3 TF/GLAD In_2O_3 VNS interface, as determined using the following equation.

$$I_0 = A^* T^2 \exp\left[\frac{-q\emptyset_B}{kT}\right] \tag{5}$$

where I_0 is the reverse saturation current corresponding to zero bias, A^* is the Richardson constant, k is the Boltzmann constant, $\emptyset_B$ is the zero-bias barrier height, q is the elementary charge, and T is the temperature.[43] The barrier height decreased for the of n-Si/In_2O_3 TF/GLAD In_2O_3 VNS device, which favors tunneling of the charge carriers[43] compared to the n-Si/In_2O_3 TF device.

The detectivity of the photodetector can be extracted from the *ln*(*I*)–*V* characteristics using the following equation,

$$D* = \frac{R}{\sqrt{2eJ_{dark}}} \tag{6}$$

where R is the responsivity of the devices, e is the charge of an electron and J_{dark} is current density in darkness.[14] Figure 7a and b show the detectivity ($D*$) and NEP of the photodetectors at an operating voltage ranging from −8 V to 0 V. A maximum detectivity of ~12.8 × 10^7 Jones was observed for the n-Si/In_2O_3 TF/GLAD In_2O_3 VNS device compared ~0.82 × 10^7 Jones for the n-Si/In_2O_3 TF device at −1.7 V, a ~15.6-fold enhancement in detectivity, which may be attributed to the efficient photogating effect in the depletion region of the VNS device.[44] A NEP of ~0.6 × 10^{-12} watts was calculated for the n-Si/In_2O_3 TF/GLAD In_2O_3 VNS device, whereas the NEP for the In-Si/In_2O_3 TF device was ~7 × 10^{-12} watts, a ~11.6-fold lower NEP, which

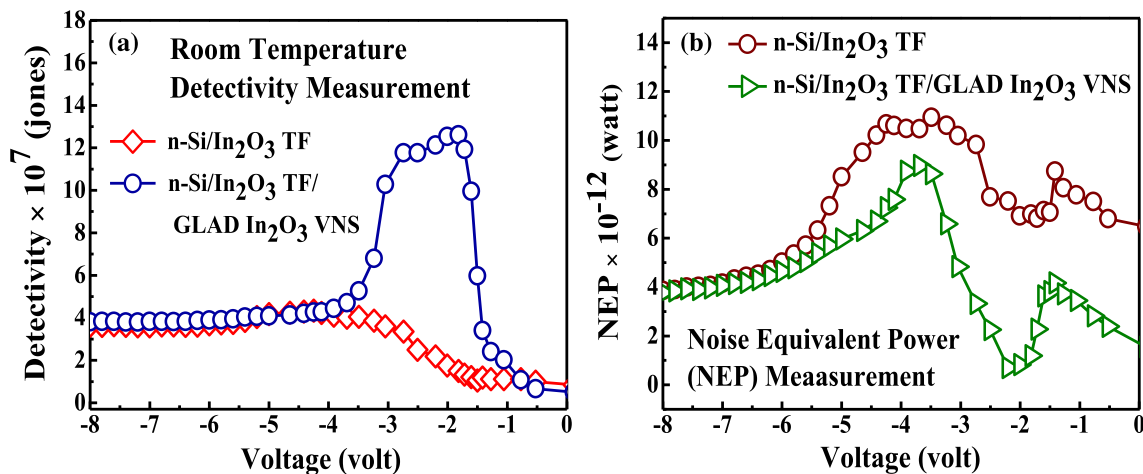

Fig. 7 (a) Detectivity, (b) *NEP* of the devices.

Table II Comparison of different parameters reported in this work and other reported works

Sl. No.	Device structures	Detectivity (Jones)	Noise-equivalent power (NEP) (watt)	Reference
1	n-Si/In_2O_3 TF/GLAD In_2O_3 VNS-based photodetectors	12.8×10^7	0.6×10^{-12}	This work
2	GaN Schottky barrier photodetectors	1.57×10^7	9.95×10^{-8}	46
3	MgZnO nanorod-based photodetectors	2.7×10^6	1.8×10^{-6}	47
4	GaSb NW-based capacitive photodetectors	2.7×10^7	11.6×10^{-9}	48
5	AlGaN/GaN metal-semiconductor-metal photodetectors	2.85×10^7	1.62×10^{-8}	49
6	Nc-Si:H film-based photodetectors	5.5×10^4	–	50
7	WSe_2 single crystal, in thin-film heterojunction photodetectors	10^7	–	51
8	In_2O_3 NW-based photodetectors	9.9×10^7	4.5×10^{-12}	52

is lower than the previously reported values.[45] The different parameters reported in this work and other reported works are depicted in Table II. Therefore, all the photodetection properties show the enormous potential of the n-Si/In_2O_3 TF/GLAD In_2O_3 VNS device as an excellent photodetector in the field of photonics technology.

Conclusion

In conclusion, the GLAD technique was employed to fabricate In_2O_3 VNS upon the In_2O_3 TF over the n-Si substrate. The SAED pattern and HRXRD analysis confirmed that the as-grown VNS were amorphous in nature. A large ~4.5-fold enhancement in absorption was observed, and a microscopic origin was proposed for the observed bandgap changes due to the surface related trap states or oxygen vacancies in the structures. The n-Si/In_2O_3 TF/GLAD In_2O_3 VNS device shows higher illumination current in the reverse-bias condition and enhancement in the ideality factor as compared to the n-Si/In_2O_3 TF device. Overall, a ~1.7-fold improvement in photosensitivity, high detectivity, and low NEP was observed in the VNS device. Therefore, the n-Si/In_2O_3 TF/GLAD In_2O_3 VNS device can be used as a low cost and high-efficiency photodetector for various potential applications.

Acknowledgments The authors want to thank Central Instrumentation Centre, Tripura University, India and Centre of Excellence in Advanced Materials, NIT Durgapur, India for providing FESEM facility, and Dr. B. Saha of NIT Agartala for the optical absorption measurement facility.

Funding This research was funded by NIT Agartala.

Conflict of interest The authors declare that they have no conflict of interest.

References

1. H. Sabet, B.C. Stack, and V.V. Nagarkar, *IEEET Nucl. Sci.* 62, 1927 (2015).
2. T. Dixit, J. Agrawal, K.L. Ganapathi, V. Singh, and M.S. Ramachandra-Rao, *IEEE Electron Device Lett.* 40, 1143 (2019).
3. S. Zhang, L. Cai, T. Wang, R. Shi, J. Miao, L. Wei, Y. Chen, N. Sepúlveda, and C. Wang, *Sci. Rep.* 5, 17883 (2015).
4. W.W. Moses, *Nucl. Instrum. Meth. A* 610, 11 (2019).
5. G. Bae et al., in IEEE International Electron Devices Meeting (IEDM), San Francisco, 28.7.1-28.7.4 (2018).
6. P. Erhart, A. Klein, R.G. Egdell, and K. Albe, *Phys. Rev. B* 75, 153205 (2007).
7. A. Nath, B.K. Mahajan, and M.B. Sarkar, *IEEE Trans. Nanotechnol.* 19, 856 (2020).
8. V.K. Yadav, A. Nath, A. Das, J.T. Mazumder, and M.B. Sarkar, *IEEE Electron Device Lett.* 42, 192 (2021).
9. P. Pooja, and P. Chinnamuthu, *IEEE Trans. Nanotechnol.* 19, 34 (2020).
10. R. Raman, A. Nath, and M. B. Sarkar, in Soft Computing: Theories and Applications, Advances in Intelligent Systems and Computing, ed. By Millie Pant, Tarun Kumar Sharma, Rajeev Arya, B. C. Sahana, Hossein Zolfagharinia (Springer Nature Singapore Pte Ltd., 2020), p. 555.
11. M.M. Hawkeye, and M.J. Brett, *J. Vac. Sci. Technol. A* 25, 1317 (2007).
12. C. Ghosh, S.M.M.D. Dwivedi, A. Ghosh, A. Dalal, and A. Mondal, *Appl. Phys. A* 125, 810 (2019).
13. S.D. Han, M.-S. Noh, S. Kim, Y.-S. Shim, Y.G. Song, K. Lee, H.R. Lee, S. Nahm, S.-J. Yoon, J.-S. Kim, and C.-Y. Kang, *Sens. Actuators B Chem.* 248, 894 (2017).
14. A. Nath, and M.B. Sarkar, *Plasmonics* 16, 37 (2021).
15. K.A. Ann-Mary, N.V. Unnikrishnan, and R. Philip, *RSC Adv.* 5, 14034 (2015).
16. K. Anand, J. Kaur, R.C. Singh, and R. Thangaraj, *Ceram. Int.* 42, 10957 (2016).
17. A. Nath, R. Raman, V.K. Yadav, P. Sannibabu, and M.B. Sarkar, *J. Nanosci. Nanotechnol.* 20, 7668 (2020).
18. K. Robbie, and M.J. Brett, *J. Vac. Sci. Technol. A* 15, 1460 (1997).
19. B.K. Mahajan, B. Choudhuri, D. Goswami, A.K. Tiwari, M.B. Sarkar, and A. Mondal, *J. Nanosci. Nanotechnol.* 20, 2344 (2020).
20. B. Choudhuri, A. Mondal, and A. Saha, *J. Electron. Mater.* 45, 4208 (2016).

21. R. Kumar, M.A. Khan, A.V. Anupama, S.B. Krupanidhi, and B. Sahoo, *Appl. Surf. Sci.* 538, 148187 (2021).
22. R. Kumar, A. Kumar, N. Verma, V. Khopkar, R. Philip, and B. Sahoo, *ACS Appl. Nano Mater.* 3, 8618 (2020).
23. R. Kumar, A. Kumar, N. Verma, R. Philip, and B. Sahoo, *J. Alloys Compd.* 849, 156665 (2020).
24. A. Kumar, R. Kumar, N. Verma, A.V. Anupama, H.K. Choudhary, R. Philip, and B. Sahoo, *Opt. Mater.* 108, 110163 (2020).
25. N. Bindushree, A. Dhabale, M.S. Dhanush, A. Honakeri, A. Ankit, M.K. Anusha, R. Kumar, H.K. Choudhary, V. Khopkar, K.C. Sekhar, and B. Sahoo, *Electron. Mater. Lett.* 16, 595 (2020).
26. L.N. Mahour, H.K. Choudhary, R. Kumar, A.V. Anupama, and B. Sahoo, *Ceram. Int.* 45, 24625 (2019).
27. R. Kumar, A. Kumar, N. Verma, A.V. Anupama, R. Philip, and B. Sahoo, *Carbon* 153, 545 (2019).
28. J. Tauc, R. Grigorovici, and A. Vancu, *Phys. Status Solidi B* 15, 627 (1966).
29. N. Pentyala, R.K. Guduru, E.M. Shnerpunas, and P.S. Mohanty, *Appl. Surf. Sci.* 257, 6850 (2011).
30. M.B. Sarkar, A. Mondal, B. Choudhuri, B.K. Mahajan, S. Chakrabartty, and C. Ngangbam, *J. Alloys Compd.* 615, 440 (2014).
31. J. Wang, Z. Wang, B. Huang, Y. Ma, Y. Liu, X. Qin, X. Zhang, Y. Dai, and A.C.S. Appl, *Mater. Interfaces* 4, 4024 (2012).
32. A.S. Hassanien, and A.A. Akl, *J. Alloys Compd.* 648, 280 (2015).
33. S. Mondal, C. Ghosh, S.M.M.D. Dwivedi, A. Ghosh, S. Sushama, S. Chakrabarti, and A. Mondal, *Ceram. Int.* 42, 10957 (2020).
34. V.R. Akshay, B. Arun, G. Mandal, and M. Vasundhara, *Phys. Chem. Chem. Phys.* 21, 12991 (2019).
35. Y. Chen, X.L. Xu, G.H. Zhang, H. Xuea, and S.Y. Ma, *Phys. B* 404, 3645 (2009).
36. L.M. Otto, S.L. Diedenhofen, B.C. Kaas, R.E. Algra, E.P.A.M. Bakkers, J.G. Rivas, and A. Lagendijk, *Nano Lett.* 9, 930 (2009).
37. S. Kohtani, A. Kawashima, and H. Miyabe, *Catalysts* 7, 303 (2017).
38. K. Mohanraj, D. Balasubramanian, J. Chandrasekaran, and A.C. Bose, *Mater. Sci. In Semicond. Proc.* 79, 74 (2018).
39. A.M. Nawar, M. Abd-Elsalam, A.M. El-Mahalawy, and M.M. El-Nahass, *Appl. Phys. A* 126, 113 (2020).
40. W.-C. Chang, S.-C. Su, and C.-C. Wu, *Materials* 9, 534 (2016).
41. A. Mondal, B.K. Mahajan, B. Choudhuri, A.K. Tiwari, S. Chakrabarty, and K.K. Chattopadhyay, *J. Nanophoton.* 8, 083069 (2014).
42. Z. Yuan, *Phys. E.* 56, 160 (2014).
43. H. Zheng, B.K. Mahajan, S.C. Su, S. Mukherjee, K. Gangopadhyay, and S. Gangopadhyay, *Sci. Rep.* 6, 25234 (2016).
44. N. Guo, F. Gong, J. Liu, Y. Jia, S. Zhao, L. Liao, M. Su, Z. Fan, X. Chen, W. Lu, L. Xiao, W. Hu, and A.C.S. Appl, *Mater. Interfaces* 9, 34489 (2017).
45. C. Yu, Z. Huang, G. Lin, Y. Mao, H. Hong, L. Zhang, Y. Zhao, J. Wang, W. Huang, S. Chen, and C. Li, *J. Phys. D: Appl. Phys.* 53, 125103 (2020).
46. T.-P. Chen, S.-J. Young, S.-J. Chang, B.-R. Huang, S.-M. Wang, C.-H. Hsiao, S.-L. Wu, and C.-B. Yang, *IEEE Sens. J.* 12, 2824 (2012).
47. S.-J. Young, and Y.-H. Liu, *Sens. Actuator A Phys.* 269, 363 (2018).
48. S. Bandyopadhyay, *J. Appl. Phys.* 116, 023108 (2014).
49. K.H. Lee, P.C. Chang, S.J. Chang, Y.C. Wang, C.L. Yu, and S.L. Wu, *IEEE. Sens. J.* 9, 723 (2009).
50. V. Jadkar, A. Pawbake, A. Jadhavar, R. Waykar, S. Pandharkar, A. Bhorde, R. Aher, S. Nair, B. Gabhale, A. Waghmare, D. Naik, P. Vairale, S. Gosavi, and S. Jadkar, *ES Mater. Manuf.* 5, 57 (2019).
51. V. Dixit, S. Nair, J. Joy, C.U. Vyas, A.B. Patel, P. Chauhan, C.K. Sumesh, S. Narayan, P.K. Jha, G.K. Solanki, K.D. Patel, and V.M. Pathak, *Eur. Phys. J. B* 92, 118 (2019).
52. A. Nath, R. Raman, L.R. Singh, and M.B. Sarkar, *J. Nanosci. Nanotechnol.* 21, 3115 (2021).

Publisher's Note Springer Nature remains neutral with regard to jurisdictional claims in published maps and institutional affiliations.